Available online at www.sciencedirect.com

SCIENCE DIRECT®

Earth and Planetary Science Letters 226 (2004) 507–519

EPSL

www.elsevier.com/locate/epsl

In situ observation of texture development in olivine, ringwoodite, magnesiowüstite and silicate perovskite at high pressure

H.-R. Wenk[a,*], I. Lonardelli[a], J. Pehl[a], J. Devine[b], V. Prakapenka[c], G. Shen[c], H.-K. Mao[d]

[a]*Department of Earth and Planetary Science, University of California, Berkeley, CA 94720, United States*
[b]*Department of Geophysical Science, University of Chicago, Chicago, IL 60637, United States*
[c]*APS, GSECARS, Argonne, IL 60139, United States*
[d]*Geophysical Laboratory, Carnegie Institution, Washington, DC 20015, United States*

Received 16 January 2004; received in revised form 20 July 2004; accepted 20 July 2004
Available online 11 September 2004
Editor: S. King

Abstract

Magnesium silicates are the dominant minerals in the earth's mantle. Their preferred orientation is important for understanding the rheology and seismic anisotropy in the deep earth. Here we report results of radial synchrotron diffraction diamond anvil cell (DAC) experiments on San Carlos olivine, axially compressed to 50 GPa. Experiments were performed at room temperature, except for brief laser heating to induce phase transformations. High stresses and development of preferred orientation were observed in diffraction images. Quantitative texture information was obtained by analyzing the images with the Rietveld method. With increasing pressure (between 9 and 43 GPa) olivine develops a texture with [001] axes perpendicular to the compression direction that is compatible with {hk0}[001] pencil glide. Ringwoodite (between 20 and 50 GPa) develops weak preferred orientation with {011} lattice planes perpendicular to the compression direction. After the phase transformation, perovskite and magnesiowüstite display transformation textures that are then modified by continuing deformation. Magnesiowüstite has a weak ⟨111⟩ maximum parallel to the compression direction that changes towards ⟨001⟩ with increasing deformation. Perovskite, transforming from olivine, has a pronounced (100) transformation texture and with increasing deformation a {012} maximum develops. The transformation texture is probably produced by mechanical {110} twinning and nucleation in orientations that minimize elastic strain energy. The deformation texture of perovskite is due to slip.

Keywords: preferred orientation; perovskite; olivine; diamond anvil cells; mantle anisotropy; Rietveld image analysis

1. Introduction

Ever since seismic anisotropy was first documented in the shallow upper mantle beneath oceans

* Corresponding author. Tel.: +1 510 642 7431; fax: +1 510 643 9980.
E-mail address: wenk@seismo.berkeley.edu (H.-R. Wenk).

0012-821X/$ - see front matter © 2004 Elsevier B.V. All rights reserved.
doi:10.1016/j.epsl.2004.07.033

[1], geophysicists have been concerned with implications of this feature for interpretation of seismic signals as well as an indicator of flow patterns in the deep earth. Maps of azimuthal anisotropy have been constructed for the uppermost mantle beneath oceanic lithosphere [2]. Fast wave propagation directions overall correspond to flow directions as implied from plate motions. Hess attributed anisotropy to preferred orientation of olivine that was attained during mantle convection. This concept has generally been accepted and is supported by quantitative polycrystal plasticity simulations (e.g. [3,4]).

The anisotropy pattern has been refined and it became apparent that anisotropy in the upper mantle varies not only laterally but also with depth [5]. Overall, anisotropy at 200 km is weaker than at 100 km. Anisotropy is at a deeper level beneath continents than oceans and less pronounced. It corresponds to assumed convection cells with upwelling and subduction. Anisotropy was also documented in layers of the transition zone (400–700 km) where olivine breaks down to high-pressure phases. Particularly just above the 660 km discontinuity anisotropy is pronounced and may be related to intense deformation associated with those phase transitions [6,7].

There is little evidence for anisotropy between 700 and 2700 km (a few exceptions have been noted [8]), but this may be partially due to limited crossing ray coverage. However, the deep mantle, in the vicinity of the boundary with the core (D″ layer), reveals itself as a fascinating and heterogeneous area of the earth (e.g. [9]). Geodynamic modeling suggests very strongly deformed subducting slabs [10] and seismologists have observed anisotropy that could be due to texturing (e.g. [11–15]), periodic layering [16], or partial melt [17].

The deformation behavior of olivine, the main constituent of the upper mantle, is fairly well understood. However, the high-pressure phases that compose the transition zone and lower mantle are much more enigmatic. Ordinary deformation experiments cannot be performed at the high pressures and temperatures corresponding to the lower mantle, though new multianvil apparatuses can deform materials up to 40 GPa [18]. Also, some of the phases cannot be quenched and recovered, and in situ analysis is necessary. In this study, we are using radial diamond anvil diffraction experiments to document in situ texture and stress development in magnesium silicates. The objective was to investigate what happens to olivine when it transforms to high-pressure phases under stress.

The $(Mg,Fe)_2SiO_4$ pressure temperature phase diagram is well established, both with experiments [19] and theory [20]. At room temperature, the equilibrium phase boundary between pure forsterite and a spinel-like structure of ringwoodite is at 10 GPa. The boundary between the ringwoodite stability field and that of perovskite ($MgSiO_3$) and periclase (MgO) is at 26 GPa. With increasing iron content, the phase boundary shifts towards lower pressure. However, for kinetic reasons these phase transformations do not occur at room temperature and heating to approximately 1000 °C is required.

These new experiments shed light on processes during phase transformations at high pressure and provide information about deformation mechanisms. They document that even at room temperature these silicates and oxides undergo plastic intracrystalline deformation. We realize that the results we report are only a first step and there is no claim that the low temperature, high stress experiments have any direct implications for the rheology of these phases in the mantle. Nevertheless, they prepare us for the investigation of mechanisms and particularly are excellent material for developing novel quantitative methods of data analysis.

2. Experiments

Magnesium-rich olivine is the main constituent of the upper mantle. Thus we chose San Carlos olivine (90.7% forsterite, 9.3% fayalite [21]) as a starting material. A fine powder was prepared (<5 μm). Two experiments were performed with a customized symmetric diamond anvil cell (DAC) with radial diffraction cones machined to an opening angle of 37° (radius). A confining gasket was prepared with an amorphous boron and epoxy composite. Residual diffraction lines at low angles suggest that the gasket material was not completely amorphous. The sample was assembled in a 100-μm hole drilled into the gasket, which had been pre-indented to a thickness of 20 μm. The sample was approximately 30 μm in thickness and was centered on the 250 μm diamond culets. A small amount of gold was positioned at the top of the assembly and served to

locate the position of the specimen as well as for pressure calibration. The assembly procedure is delicate and several gaskets failed during the assembly. In the first experiment, gasket material intruded and covered the olivine powder. For the second experiment, more olivine powder was available but transformations were less homogeneous.

The DAC was then used for diffraction experiments at the ID-13 beamline of the GSECARS sector at the Advanced Photon Source at Argonne National Laboratory. A monochromatic X-ray beam (λ=0.3311 Å), approximately 7–8 μm in diameter, was focused on the DAC assembly in radial geometry with the DAC axis horizontal and at right angles to the incident beam. Diffraction images were recorded with a 2048×2048 pixel MAR-CCD camera in 2k mode with 16 bit dynamic range. The camera was mounted at 28.3 cm from the sample, thus optimizing the range of diffractions recorded for the opening cone of the DAC to $2\theta_{max}$=14.5° or d_{min}=1.3 Å. The sample–detector distance was calibrated with a CeO_2 standard.

Three exposures were taken at each condition: a first one, centered on the gold, was used to establish the hydrostatic pressure based on the elastic deformation of the gold lattice [22,23]. For the second exposure, the beam was centered on the sample (Fig. 1a), and for the third, the beam passed through the diamond, near the sample interface (Fig. 1b). The latter exposure was taken to get a background image for scattering from gasket and sample assembly that was subsequently subtracted from the sample image (Fig. 1c). As is obvious from Fig. 1, in radial diffraction scattering from the gasket is substantial and only after background subtraction details of the sample diffraction pattern are revealed, including intensity variations along Debye rings that are indicative of preferred orientation. Even in the background-subtracted image the remaining background is substantial. Exposure times ranged from 30 to 90 s. Longer exposure times could not be used because the CCD camera saturated due to the high background. When background-subtracted images are "caked" in FIT2D [24], transforming the circular image into a square plot, the presence of texture becomes immediately obvious by visual inspection of intensity variations with azimuth, as is illustrated for an example with ringwoodite (Fig. 2a) and perovskite+magnesiowüstite (Fig. 2b). The sinusoidal variations of the diffraction lines (well visible in Fig. 2a) are an expression of elastic distortions due to applied stress. The position of the compression direction (diamond axis) is indicated on the figures (smaller d-spacings, larger 2θ).

After each measurement, the DAC was removed from the goniometer to manually increase pressure, then inserted again and centered, using gold as a reference. Phase transformations had to be induced by laser heating. Radial laser heating, with the DAC axis mounted parallel to the direction of the beam, was performed at GSECARS. Temperatures reached during the axial heating events were estimated to be around 1000 °C. Conditions for the experiments are summarized in Fig. 3. The two experimental suites were done in parallel over 3 days. After each heating step, the confining pressure dropped slightly. In experiment 1, the pressure was further reduced after the second heating step and then increased again to

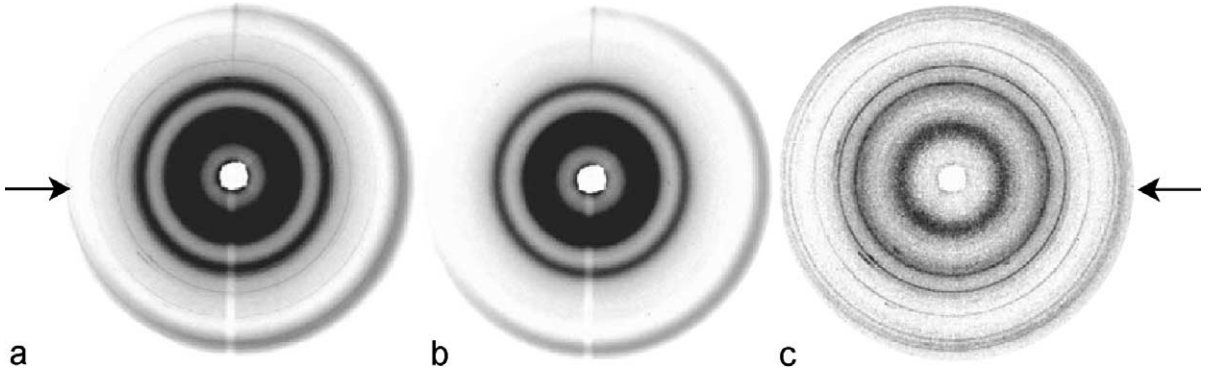

Fig. 1. Synchrotron diffraction images for experiment 1 at 43 GPa. (a) Beam focused on sample (intensity: maximum 23,000; minimum 6000), (b) background (intensity: maximum 22,000; minimum 6000), (c) subtracted (intensity: maximum 1300; minimum 200).

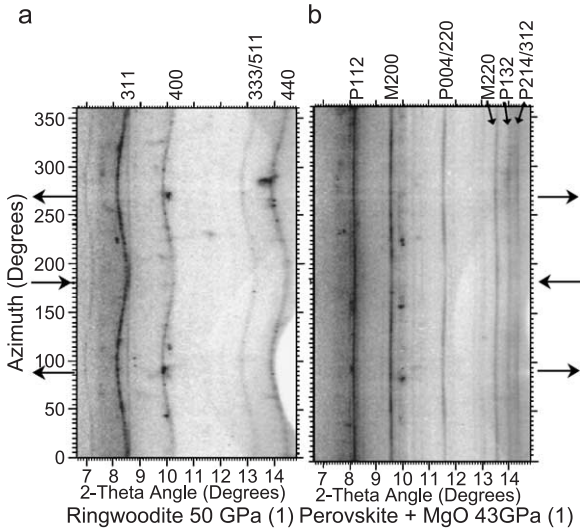

Fig. 2. Synchrotron diffraction images from experiment 1, "caked" with FIT2D. Some diffraction peaks are labeled. (a) 50 GPa, ringwoodite with sinusoidal peak shifts due to axial stress, (b) 43 GPa after heating to induce phase transformation, perovskite (P)+magnesiowüstite (M) (c.f. Fig. 1). Vertical axis is azimuth, horizontal axis is diffraction angle 2θ. Compression direction (diamond axis) and extension direction are indicated by arrows.

produce deformation of perovskite. In experiment 2, the equilibrium pressure for ringwoodite was overshot and olivine transformed largely to perovskite+magnesiowüstite at 43 GPa.

Most of the diffraction images were very complex with a poor peak to background ratio (even after background subtraction) often with multiple phases and many overlapping peaks. A simple intensity extraction along Debye rings as used previously [25,26] was not possible. Thus we decided to use

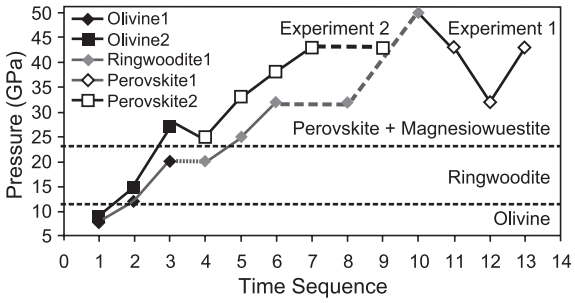

Fig. 3. Experimental conditions. Dotted lines indicate events of laser heating, dashed lines indicate where the sample was left for an extended period. The equilibrium stability boundaries for the mineral assemblages are indicated by horizontal dashed lines. The horizontal axis indicates the progression of the experiments and is not proportional to real time.

the Rietveld method as implemented in the program system MAUD [27] to analyze background-subtracted images. Three approaches were tested and compared: the first was to enter experimental images directly into MAUD, making use of a new capability. The program refines the center of the images and then calculates integrated diffraction profiles over angular slices (10° was chosen for the present analysis, resulting in 36 profiles). The second approach used FIT2D, first correcting images for distortion with a CeO_2 standard, then integrating intensities in 5° segments over a 90° sector for images where only a single phase was present (resulting in 19 profiles), or over the full circle (72 profiles) in cases with multiple phases. FIT2D was used for the graphical representations in Figs. 1 and 2. Fig. 4 shows a stack of 36 profiles for experiment 1, 19 GPa, in 10° intervals. Most diffraction peaks can be assigned to olivine, with intensity variations and systematic shifts in positions of peaks. These profiles served as input for the Rietveld analysis. For a few images, we also used the conventional procedure, extracting intensities for some diffraction rings directly and processing the data with the BEARTEX program [28] to obtain the orientation distribution. BEARTEX was used for calculations of inverse pole figures and for graphical texture representations.

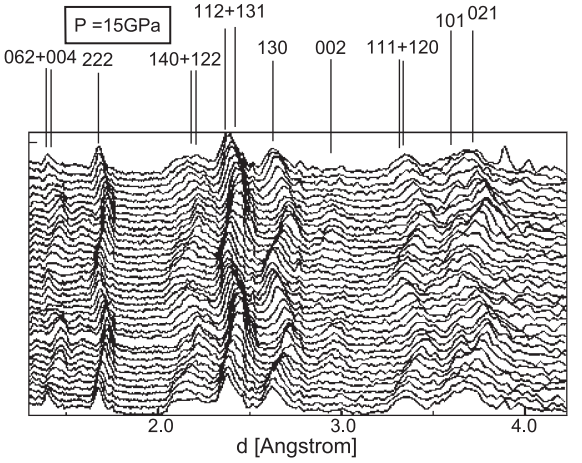

Fig. 4. Stack of 36 diffraction profiles in different radial directions (10° intervals) for experiment 2, olivine at 15 GPa. Note variations in peak positions and peak intensities.

The Rietveld procedure used all diffraction profiles in the range 1.5 to 3.5 Å, refining first instrumental parameters (detector distance, image center, peak profile, overall intensity), background parameters, crystallographic parameters of phases (lattice parameters, atomic coordinates) and finally phase proportion, texture (using the harmonic method and the direct method EWIMV [27], based on tomography), and stress (using a simple isotropic triaxial stress model). For the texture calculation, axial symmetry around the DAC axis was assumed. This is justified because of the axial geometry of the experiment. It is corroborated by similar intensity variations in the four equivalent sectors of the Debye rings and a single 90° sector would in principle provide sufficient information. However, there are minor deviations in the intensity variations and averaging of the equivalent sectors provides a statistically more satisfactory solution. The deviations between sectors are attributed to grain statistics and to deviations from axial strain in the DAC. It must be emphasized that the Rietveld procedure was by no means "automatic". We attribute this largely to the poor peak to background ratio, with many peaks less than 1% above background, even for background subtracted images. The refinement had to be done in steps as described above, and in the case of polyphase assemblages beginning with the most abundant phase and then advancing to minor phases. In the case of these complex images, the Rietveld method was essential and we were impressed by the very consistent texture patterns that were obtained.

3. Results

Two experimental series were performed in separate diamond anvil cells, both with olivine as starting material. In the first series, olivine was deformed (in three steps) to 23 GPa. At this point, laser heating was used to transform olivine to ringwoodite. Ringwoodite was then deformed (in four steps) to 50 GPa (it was kept at 32 GPa for an extended period) and transformed (by heating) to perovskite+magnesiowüstite. Pressure was then reduced to 32 GPa, causing an extensional stress regime. With subsequent pressure increase to 43 GPa, the sample deformed again in compression.

The second series deformed olivine (in three steps) to 27 GPa overshooting the stability field of ringwoodite. The transformation to perovskite+magnesiowüstite was then induced by heating but the sample remained heterogeneous, with some olivine still present and also minor amounts of ringwoodite at the highest pressures. This assembly was then deformed in four steps to 43 GPa. At 43 GPa, the sample was left for 12 h and investigated again.

The starting material (olivine) has a fairly random orientation distribution and Debye rings are uniform, indicating a small grain size (estimated at 1–5 μm). After each heating cycle, a spot pattern develops, suggesting nucleation and growth of new grains during the phase transformation. During subsequent pressure increase, the spot pattern attenuates and intensity variations along rings become more symmetrical. Already in a visual inspection of images (such as that in Fig. 2c), the presence of texture is obvious. Strong textures have been observed in gold, olivine and perovskite. A weaker texture develops in ringwoodite and magnesiowüstite.

Fig. 5 shows two diffraction profiles for the complex sample from experiment 2 at 43 GPa with five phases. Experimental (dotted) and calculated lines document a good fit. The profile in Fig. 5 (top) is parallel to the compression direction and profile in Fig. 5 (bottom) perpendicular to it. Deviations in peak intensities are an expression of texture; deviations in peak positions are due to deviatoric stress. Note that even at these high-pressure con-

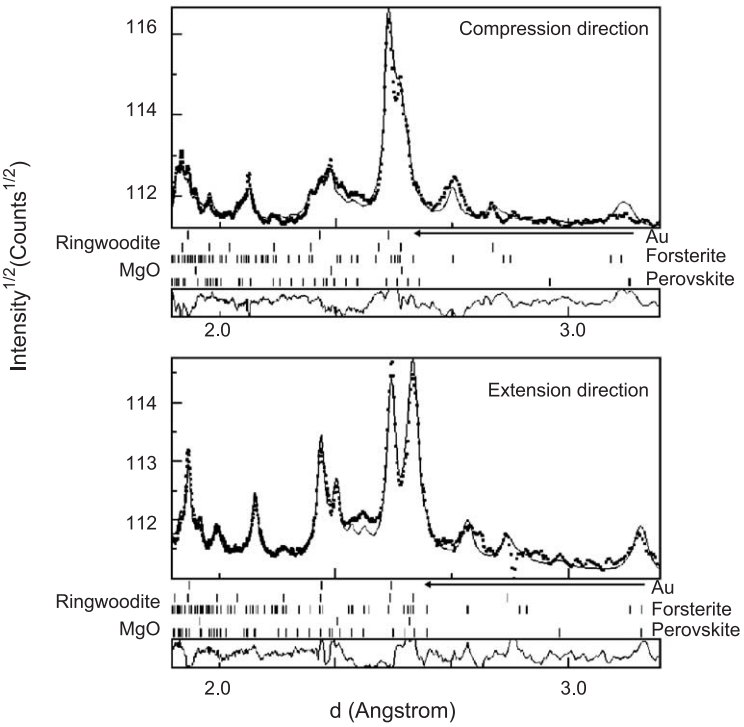

Fig. 5. Selected diffraction profiles for experiment 2 at 43 GPa. Experimental data (dots) and Rietveld fit (solid line). Top profile is in the compression direction, bottom profile in the extension direction.

ditions some olivine is still present. The reasons for the observed heterogeneity are temperature and pressure gradients that were not optimal in this experiment, particularly during the laser heating.

Some of the phase parameters that have been refined are listed in Table 1. Hydrostatic pressures have been estimated from the average lattice parameter of gold and are probably within ±1–4 GPa due to uncertainties in the equations of state for gold [23]. We also give estimated standard deviations as obtained from the least squares Rietveld refinement. They are very low and the real uncertainty may be considerably larger [29], particularly lattice parameters and stresses depend on several assumptions and corrections. However, lattice parameters for all phases are comparable with those reported in the literature. The resolution in radial diffraction is not as high as in axial diffraction because of higher background from gasket, sample heterogeneity, pressure gradients and stress that introduces line broadening. Phase proportions are compatible; especially in perovskite–magnesiowüstite containing samples volume proportions of the two phases range between 2:1 and 3:1, as would be expected. Deviatoric stresses vary between the five phases. They were refined assuming bulk moduli and Poisson's ratios given in the literature ([30] for olivine, [31,32] for ringwoodite, [31,33,34] for periclase, and [35,36] for perovskite). First deviatoric stress components σ_{11} (diamond axis), σ_{22} and σ_{33} were refined simultaneously. In all cases, σ_{11} was compressional and σ_{22} and σ_{33} extensional and almost equal, consistent with an axially symmetric stress distribution. In the final refinement, σ_{22} and σ_{33} were kept constant and only σ_{11} was refined. Highest compressive stress values (9 GPa) were observed for ringwoodite and olivine, intermediate values for perovskite and periclase and very low values for gold (0.1–0.5 GPa). This illustrates a very heterogeneous local stress distribution in this polyphase aggregate. Stresses are minimal right after phase transformations. The stresses obtained are comparable to those reported by Uchida et al. [37] in similar experiments, and for ringwoodite also to those of Kavner and Duffy [32].

Table 1
Structural parameters for various phases, refined with the Rietveld method for synchrotron diffraction images corresponding to conditions where texture information was extracted

P (GPa)	Phase	*a* (Å)	b (Å)	c (Å)	σ_{11} (GPa)	*V* (%)
Experiment 1						
50	Ringwoodite	7.6501 (4)			13.4 (3)	100
43[a]	Perovskite	4.5512 (7)	4.7253 (8)	6.5811 (8)	0.85 (2)	75.0 (2)
	Magnesiowüstite	3.9658 (2)			0.81 (3)	25.0 (1)
43[b]	Perovskite	4.5511 (7)	4.7298 (7)	6.5778 (8)	0.51 (2)	77.8 (8)
	Magnesiowüstite	3.9658 (1)			0.57 (2)	22.0 (3)
	Gold	3.8437 (2)			0.01	<1
Experiment 2						
9	Olivine	4.7067 (6)	9.9519 (9)	5.8911 (5)	2.90 (1)	100
15	Olivine	4.6650 (4)	9.7673 (8)	5.8276 (6)	5.14 (4)	100
27	Olivine	4.6192 (4)	9.5479 (9)	5.7078 (5)	7.71 (5)	100
25[a]	Olivine	4.6273 (7)	9.5812 (8)	5.7226 (7)	6.48 (5)	32.9 (3)
	Perovskite	4.6281 (7)	4.8553 (7)	6.6764 (8)	0.42 (2)	29.6 (2)
	Magnesiowüstite	4.0529 (3)			0.12 (1)	13.6 (2)
	Ringwoodite	7.7997 (4)			0.46 (2)	23.6 (2)
	Gold	3.9314 (3)			0.11 (1)	<1
43	Olivine	4.5865 (5)	9.2901 (7)	5.5834 (8)	7.30 (6)	28.0 (2)
	Perovskite	4.5810 (8)	4.7736 (4)	6.6023 (7)	4.91 (5)	31.2 (2)
	Magnesiowüstite	4.0198 (8)			5.62 (8)	14.9 (2)
	Ringwoodite	7.7604 (9)			8.72 (7)	24.1 (3)
	Gold	3.8784 (5)			0.51 (2)	1.50 (1)

Estimated standard deviations based on the least squares refinement are in parentheses. Actual uncertainties may be considerably larger.
[a] After phase transformation.
[b] After deformation.

The results of the quantitative texture analysis are represented in inverse pole figures, which display the pole densities in the compression direction relative to crystal coordinates. In inverse pole figures, the asymmetric sector corresponding to crystal symmetry is sufficient for a complete representation. We only show textures obtained directly with MAUD from 36 diffraction patterns. Those obtained from a combination of FIT2D and MAUD are similar in pattern but vary somewhat in absolute densities.

In Fig. 6, textures for the different phases at different conditions are compared. In all phases, weak to moderate texture is observed, consistent with the visual inspection of the diffraction images (such as Fig. 2c). Olivine (Fig. 6a–d) displays a broad girdle between 100 and 010 with a distinct minimum at 001 (suggesting that the *c*-axis is perpendicular to the compression direction). At the highest pressures (43 GPa), the maximum shifts towards 010 (Fig. 6d). For perovskite, two texture types have been observed. In experiment 1 and transforming from ringwoodite at 43 GPa, a 012 texture is present that increases in strength with further deformation (Fig. 6g). In experiment 2 and transforming from olivine at 25 GPa, the texture type is 100 (Fig. 6e) and this type remains to 43 GPa (Fig. 6f). Ringwoodite, after the transformation from olivine, has a fairly random orientation distribution (Fig. 6h), but with increasing pressure, a distinct 011 texture develops (Fig. 6i). The texture of magnesiowüstite is weak (Fig. 6j,k). After transformation from ringwoodite, a 111 type is observed that shifts towards 011 with increasing pressure. Gold (Fig. 6l) consistently shows a 111 fiber texture with a shoulder towards 011 in both experiments and at all conditions. The gold texture does not change much with increasing pressure.

4. Discussion

These new high-pressure deformation textures can be compared with earlier deformation experi-

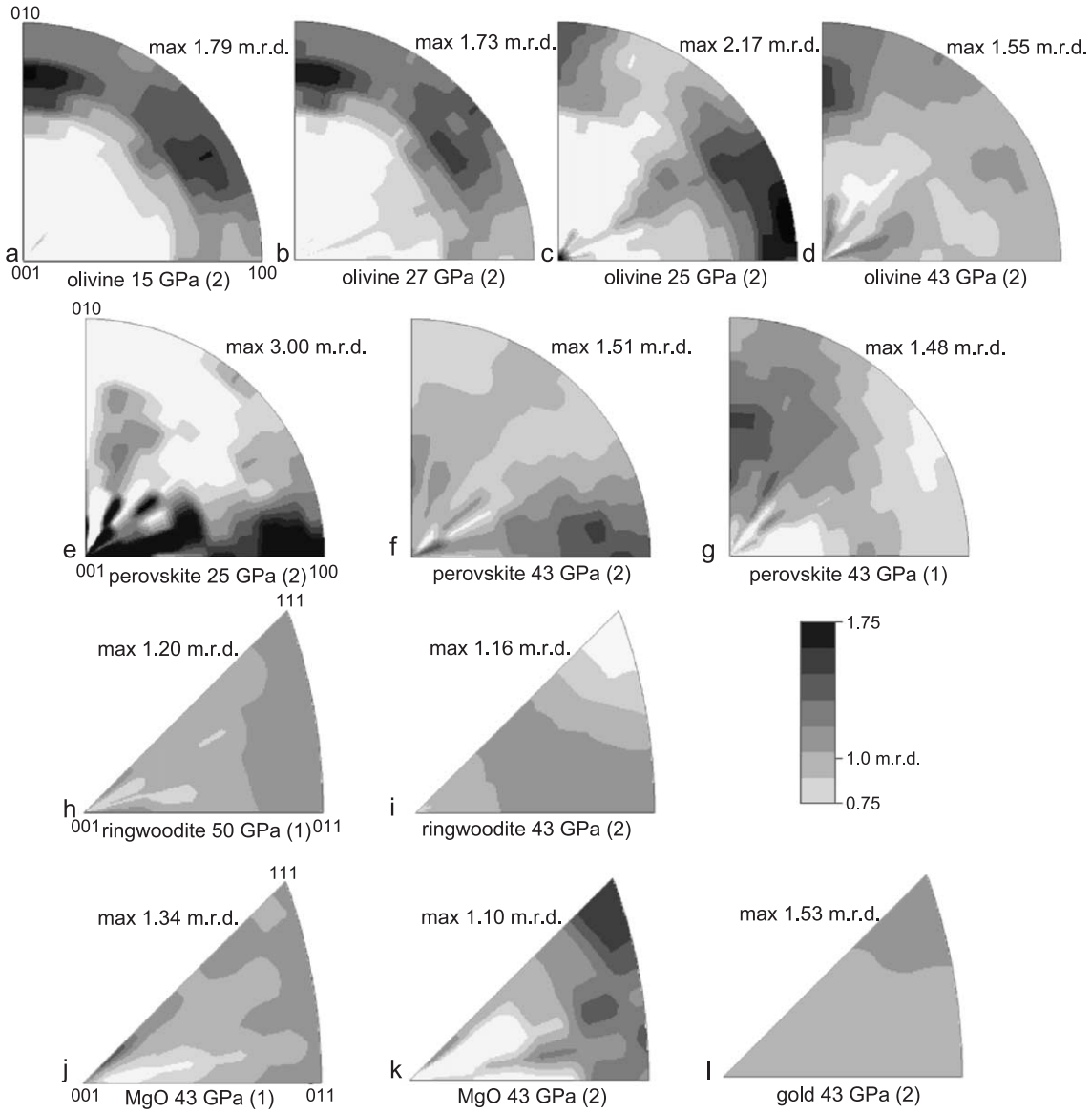

Fig. 6. Inverse pole figures for different phases. (a–d) Olivine, experiment 2; (a) 15 GPa, (b) 27 GPa, (c) 25 GPa (after transformation), (d) 43 GPa. (e–g) Perovskite; (e) 25 GPa (after transformation, experiment 2), (f) 43 GPa (experiment 2), (g) 43 GPa (experiment 1). (h,i) Ringwoodite; (h) 50 GPa (experiment 1), (i) 43 GPa (experiment 2, harmonic method). (j,k) Magnesiowüstite, (j) 43 GPa (experiment 1), (k) 43 GPa (experiment 2, harmonic method). (l) Gold, 43 GPa (experiment 2). All results are for EWIMV texture extraction unless indicated. Equal area projection, linear density scale, dark shades are high densities.

ments in axial compression with diamond anvil cells, as well as other methods. We will briefly discuss the texture of gold, and then analyze texture development in olivine, ringwoodite, magnesiowüstite and perovskite.

Gold shows a strong and consistent 111 texture (Fig. 6l). This is surprising since it corresponds to a texture typical of extension for fcc metals. For compression, one would have expected a 110 fiber texture [38]. Our interpretation is that gold is the

weakest phase in the system (low deviatoric stress) and that the compressive stress is largely maintained by silicates and oxides so that gold actually deforms in tension, imposed by confining pressure. To ascertain this, micromechanical modeling would be needed and new experiments are under way.

High temperature deformation experiments on olivine produce textures with [010] poles parallel to the compression direction and [100] axes at high angles (e.g. [39]). This has been explained as due to activity of the (010)[100] slip system established in single crystal experiments [40]. The new inverse pole figures (Fig. 6a–d) also show a concentration at (010) but with a girdle towards (100) and a minimum at (001). This is consistent with the qualitative DAC experiments of Meade et al. [41]. At lower temperature, (100)[001] slip and {hk0}[001] pencil glide have been documented for single crystals [42]. These slip systems have also been identified at high temperature and high stress, with higher water content [43]. Polycrystal plasticity simulations with the self-consistent viscoplastic theory [44] for pencil glide produce indeed a very similar texture pattern as that observed (Fig. 7a). This leads us to conclude that olivine deforms by activation of low temperature slip systems at compressive stresses of 5–9 GPa and confining pressures of 9–43 GPa at room temperature.

When the textured olivine sample is transformed to ringwoodite (with spinel structure), a very weak (110) texture is produced. The texture strength increases somewhat during deformation to 43 and 50 GPa (Fig. 6h,i). The olivine–spinel transition with a 10% volume change has been interpreted as a martensitic

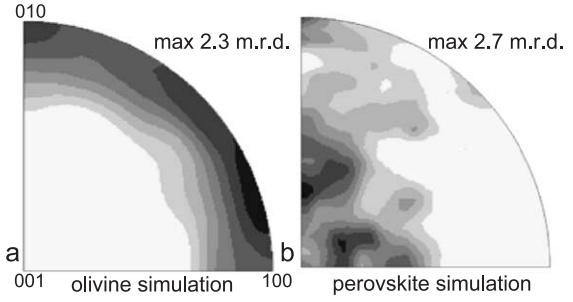

Fig. 7. Viscoplastic self-consistent simulations for deformation in axial compression to 50%, 1000 orientations (a) olivine {hk0}[001] pencil glide, (b) perovskite with (010)[100], (100)[010], and (001)⟨110⟩ slip. Inverse pole figures in equal area projection, linear contours. Dark regions are high pole densities.

(shear induced) transformation or a diffusional transformation [45–49]. The spotty diffraction pattern right after the transformation indicates an increase in grain size and growth. The weak texture precludes a strong orientation relationship between parent (olivine) and daughter (ringwoodite) as would be expected for a martensitic transition. The texture produced with increasing pressure is most likely due to slip. A combination of {111}⟨110⟩ slip and {011}⟨110⟩ slip documented for spinel structures [50] produces indeed a 011 fiber texture in analogy to halite [51].

The high-pressure phases perovskite and magnesiowüstite transformed from ringwoodite (experiment 1) as well as from olivine (experiment 2). Magnesiowüstite shows a weak (111) transformation texture (Fig. 6k) that changes during further deformation towards (011) (Fig. 6j). This is different from previous experiments of pure periclase (MgO) [25,52] where a strong (001) fiber texture was observed and attributed to {110}⟨$\bar{1}$10⟩ slip. If other slip systems were active (such as {111}, {110} and {100}, all with the [110] slip direction as established for isostructural halite at higher temperature [53]), the maximum would be at (011). At this point, it is not clear if the different deformation texture observed here is due to the chemical composition (iron content) that may favor more slip systems, or due to the fact that deformation occurred in a polyphase system. Since magnesiowüstite is a minor component and deformation is heterogeneous, the texture pattern may be greatly influenced by the plasticity of the other phases as in the case of gold. Perovskite appears more ductile and accommodates most of the strain. No microstructural information is available, e.g. to establish whether magnesiowüstite occurs as inclusions in a dominant perovskite matrix. Interestingly, 111 is the elastically weakest orientation for MgO at high pressure (Fig. 8a) and nucleation with 111 parallel to the compression direction would minimize the elastic strain energy.

The most interesting aspect of this study is the strong texture observed in silicate perovskite with (100) lattice planes perpendicular to the compression direction (Fig. 6e,f) at low pressure and transforming from olivine, and (012) perpendicular to the compression direction (Fig. 6g) at high pressure and transforming from ringwoodite. The (100) texture agrees with qualitative observations of Chen et al. [54] and is not inconsistent with some data of Merkel

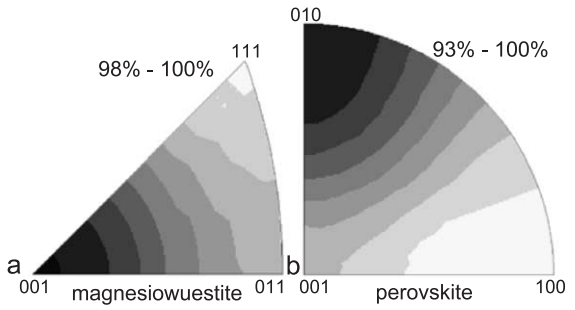

Fig. 8. Surface illustrating the anisotropy of Young's modulus for (a) MgO at 30 GPa [30], (b) silicate perovskite at 30 GPa [32]. Equal area projection. Values are normalized so that maximum is 100% (darkest region). Linear contours.

et al. [55] where their Fig. 7 indeed shows some high diffraction intensities for 200 parallel to the compression direction. One explanation for the (100) fiber texture is mechanical (110) twinning that effectively switches *a* and *b* axes, in the sense of rotating the *a*-axis towards the compression direction as observed in ferroelectric perovskites [56]. This twinning is comparable to Dauphiné twinning in quartz [57] that minimizes the elastic strain energy. Also in the case of perovskite, the 100 orientation is energetically favored over 010 (Fig. 8b).

The (012) texture may be due to slip. Slip systems are not very well known, particularly for orthorhombic perovskite. Possible slip systems (in orthorhombic setting) are (010)[100], (100)[010], and (001)⟨110⟩ [58–62]. Plasticity simulations with those systems and {010} slip slightly favored generate a texture that is remarkably similar to the observed 012 texture (Fig. 7b versus Fig. 6g). In previous radial diamond anvil experiments on $MgSiO_3$ perovskite, no texture was reported [41,55] and it has been suggested that fine-grained perovskite may be deformed by superplastic flow [63]. These new experiments clearly document intracrystalline plastic deformation for this mineral. As was mentioned above, the old data [55] may still be compatible with the new results since we are relying on a more sophisticated texture analysis.

The big advantage of radial DAC deformation experiments is that they are relatively simple and can be applied to very high pressures. There are clearly limitations, foremost the small sample volume and corresponding heterogeneity in strain; but finite element simulations [64] demonstrated that this heterogeneity is not a major concern, at least for qualitative studies, and in our case the total strains are relatively small, presumably 30–50% after compaction [25]. In the future, results from the DAC experiments should be compared with data from multianvil deformation apparatus. Such instruments [18,65] have the advantage of large sample volumes, homogeneous pressure and temperature, and particularly the possibility to separate hydrostatic pressure and deviatoric stress, though the pressure range is limited and absorption by anvil material renders the analysis of diffraction images for texture more difficult.

Compared with our previous texture studies of radial DAC images that relied on conventional peak analysis [25,55,66], we have been impressed by the powerful capabilities of the whole image Rietveld method that not only allows us to obtain simultaneously texture information for several phases, but also crystallographic parameters and stress (Table 1). The first application of this method is by no means ideal and in the future algorithms as well as image quality need to be improved. An important factor is background reduction that could be achieved with different gasket materials and gasket geometry that are presently explored. We are confident though that the Rietveld approach will become a routine method for quantitative analysis of synchrotron images.

5. Conclusions

In this study of magnesium silicates, we demonstrate that DAC experiments, though limited by sample size and deformation conditions, can provide information on the deformation behavior of the dominant minerals of the earth's lower mantle [19], including the heterogeneous and anisotropic core–mantle boundary region. The measurements give us a better understanding of mechanisms of phase transformations and provide insight into processes in the deep earth, particularly ductile deformation of mantle minerals and potential development of anisotropy. Naturally, there is uncertainty with conclusions from samples with very small grain size, deformed at room temperature and exceedingly high stresses, and we

refrain from making far-reaching direct conclusions about the rheology of the lower mantle. However, we have documented that mantle minerals can be plastically deformed in diamond anvil cells, even at room temperature, and characteristic texture patterns evolve that can be interpreted. Thus, it is likely that intracrystalline plastic deformation is also active at high temperatures in the lower mantle and could produce anisotropy during convection. Having established deformation mechanisms at low temperature, it is conceivable to use first principle approaches and dislocation dynamics to extrapolate such results to other conditions, especially high temperatures. In the future, experiments need to be performed at higher temperature and reduced stress, corresponding more closely to the conditions present in the lower mantle. With this first experiment on texture changes during phase transformations of mantle minerals, we developed procedures for a quantitative texture determination with the Rietveld method that can be applied routinely to synchrotron diffraction data.

Acknowledgements

We are appreciative for the support given by NSF, CDAC and IGPP-LANL. Discussions with L. Lutterotti, S. Merkel and S. Speziale were very valuable and thoughtful comments from reviewers improved the manuscript. We are also grateful for the access to the facilities of GSECARS at APS where the diffraction experiments were performed.

References

[1] H.H. Hess, Seismic anisotropy of the uppermost mantle under oceans, Nature 203 (1964) 629–631.
[2] J.P. Montagner, T. Tanimoto, Global upper mantle tomography of seismic velocities and anisotropies, J. Geophys. Res. 96 (1991) 20337–20351.
[3] P.R. Dawson, H.-R. Wenk, Texturing of the upper mantle during convection, Philos. Mag., A 80 (2000) 573–598.
[4] D.K. Blackman, H.-R. Wenk, J.-M. Kendall, Seismic anisotropy in the upper mantle: 1. Factors that affect mineral texture and effective elastic properties, Geochem. Geophys. Geosyst. 3 (2002) 10.1029.
[5] J.P. Montagner, L. Guillot, Seismic anisotropy and global dynamics, in: S.-I. Karato, H.-R. Wenk (Eds.), Plasticity of Minerals and Rocks, Reviews in Mineralogy and Geochemistry, Mineral. Soc. America, Washington, D.C., 2002, pp. 353–385.
[6] J. Trampert, H.J. Heijst, Global azimuthal anisotropy in the transition zone, Science 296 (2002) 1297–1299.
[7] M.J. Fouch, K.M. Fisher, Mantle anisotropy beneath northwest Pacific subduction zones, J. Geophys. Res. 101 (1996) 15987–16002.
[8] G. Barruol, R. Hoffman, Upper mantle anisotropy beneath the GEOSCOPE stations, J. Geophys. Res. 104 (1999) 10757–10774.
[9] L.H. Kellogg, B.H. Hager, R.D. van der Hilst, Compositional stratification in the deep mantle, Science 283 (1999) 1881–1884.
[10] A.K. McNamara, S.-I. Karato, P.E. van Keken, Localization of dislocation creep in the lower mantle: implications for the origin of seismic anisotropy, Earth Planet. Sci. Lett. 191 (2001) 85–99.
[11] M.J. Fouch, K.M. Fisher, M.E. Wysession, Lowermost mantle anisotropy beneath the Pacific: imaging the source of the Hawaiian plume, Earth Planet. Sci. Lett. 190 (2001) 167–180.
[12] J.M. Kendall, P.G. Silver, Constraints from seismic anisotropy on the nature of the lowermost mantle, Nature 381 (1996) 409–412.
[13] J. Ritsema, Evidence for shear velocity anisotropy in the lowermost mantle beneath the Indian Ocean, Geophys. Res. Lett. 27 (2000) 1041–1044.
[14] C. Thomas, J.-M. Kendall, The lowermost mantle beneath northern Asia: II. Evidence for lower-mantle anisotropy, Geophys. J. Int. 151 (2002) 296–308.
[15] L. Vinnik, L. Breger, B. Romanowicz, Anisotropic structures at the base of the earth's mantle, Nature 393 (1998) 564–567.
[16] E.J. Garnero, Lower mantle heterogeneity, Annu. Rev. Earth Planet. Sci. 28 (2000) 509–537.
[17] T. Lay, Q. Williams, E.J. Garnero, The core–mantle boundary layer and deep Earth dynamics, Nature 392 (1998) 461–468.
[18] W.B. Durham, D.J. Weidner, S.-I. Karato, Y. Wang, New developments in deformation experiments at high pressure, in: S.-I. Karato, H.-R. Wenk (Eds.), Plastic Deformation in Minerals and Rocks, Reviews in Mineralogy, vol. 51, Mineralogical Society of America, Washington, D.C., 2002, pp. 21–49.
[19] E. Ito, E. Takahashi, Post spinel transformations in the system Mg_2SiO_4–Fe_2SiO_4 and some geophysical implications, J. Geophys. Res. 94 (1989) 10637–10646.
[20] Y.W. Fei, S.K. Saxena, Internally consistent thermodynamic data and equilibrium phase-relations for compounds in the system MgO–SiO_2 at high-pressure and high-temperature, J. Geophys. Res. 95 (B5) (1990) 6915–6928.
[21] F.A. Frey, M. Prinz, Ultramafic inclusions from San-Carlos, Arizona—petrologic and geochemical data bearing on their petrogenesis, Earth Planet. Sci. Lett. 38 (1978) 129–176.
[22] O.L. Anderson, D.G. Isaak, S. Yamamoto, Anharmonicity and the equation of state for gold, J. Appl. Phys. 65 (1989) 1534–1543.
[23] T.S. Duffy, G. Shen, D.L. Heinz, J. Shu, Y. Me, H.K. Mao, R.J. Hemley, A.K. Singh, Lattice strains in gold and rhenium

under non-hydrostatic compression to 37 GPa, Phys. Rev., B 60 (1999) 15063–15073.
[24] A.P Hammersley, Fit2D: V99.129 Reference Manual Version 3.1. Internal Report ESRF-98-HA01, 1998.
[25] S. Merkel, H.-R. Wenk, J. Shu, G. Shen, G. Gillet, H.-K. Mao, R.J. Hemley, Deformation of polycrystalline MgO at pressures of the lower mantle, J. Geophys. Res. 107 (2002) 2271.
[26] H.-R. Wenk, S. Grigull, Synchrotron texture analysis with area detectors, J. Appl. Crystallogr. 36 (2003) 1040–1049.
[27] L. Lutterotti, MatthiesH.-R. Wenk, MAUD: a friendly Java program for materials analysis using diffraction, Int. Union Crystallogr. Comm. Powder Diffr. Newsl. 21 (1999) 14–15.
[28] H.-R. Wenk, S. Matthies, J. Donovan, D. Chateigner, BEARTEX, a Windows-based program system for quantitative texture analysis, J. Appl. Crystallogr. 31 (1998) 262–269.
[29] R.A. Young, The Rietveld Method, Oxford University Press, Oxford, 1993, 298 pp.
[30] C.S. Zha, T.S. Duffy, R.T. Downs, H.K. Mao, R.J. Hemley, Brillouin scattering and X-ray diffraction of San Carlos olivine: direct pressure determination to 32 GPa, Earth Planet. Sci. Lett. 159 (1998) 25–33.
[31] B.B. Karki, L. Stixrude, R.M. Wentzcovitch, High pressure elastic properties of major materials of earth's mantle from first principles, Rev. Geophys. 39 (2001) 507–534.
[32] A. Kavner, T.S. Duffy, Strength and elasticity of ringwoodite at upper mantle pressure, Geophys. Res. Lett. 28 (2001) 2691–2694.
[33] T.S. Duffy, R.J. Hemley, H.K. Mao, Equation of state and shear strength at multimegabar pressures: magnesium oxide to 227 GPa, Phys. Rev. Lett. 74 (1995) 1371–1374.
[34] D.L. Weidner, L. Li, M. Davis, J. Chen, Effect of plasticity on elastic modulus measurements, Geophys. Res. Lett. 31 (2004) L06621.
[35] B. Kiefer, L. Stixrude, R.M. Wentzcovitch, Elasticity of (Mg,Fe)SiO_3-perovskite at high pressures, Geophys. Res. Lett. 29 (2002) DOI:10.1029/2002GLO14683.
[36] R.M. Wentzcovitch, B.B. Karki, S. Karato, C.R.S. Da Silva, High pressure elastic anisotropy of $MgSiO_3$ perovskite and geophysical implications, Earth Planet. Sci. Lett. 164 (1998) 371–378.
[37] T. Uchida, N. Funamori, T. Ohteni, T. Yagi, Differential stress of MgO and Mg_2SiO_4 under uniaxial stress field: variation with pressure, temperature and phase transition, in: W.A. Trzeciekowski (Ed.), "High Pressure Science and Technology" Proc. Joint XV AIRAPT and XXXIII EHPRG International Conference, World Scientific, Singapore, 1996, pp. 183–185.
[38] M.G. Stout, J.S. Kallend, U.F. Kocks, M.A. Przystupa, A.D. Rollett, Material dependence of deformation texture development in various deformation modes, in: J.S. Kallend, G. Gottstein (Eds.), Eighth Int. Conf. on Textures of Materials, The Metallugical Society, Warrendale, PA, 1998, pp. 479–484.
[39] A. Nicolas, F. Boudier, A.-M. Boullier, Mechanisms of flow in naturally and experimentally deformed peridotites, Am. J. Sci. 273 (1973) 853–876.
[40] Q. Bai, S.J. Mackwell, D.L. Kohlstedt, High temperature creep of olivine single crystals: I. Mechanical results for buffered samples, J. Geophys. Res. 96 (1991) 2441–2463.
[41] C. Meade, P.G. Silver, S. Kaneshima, Laboratory and seismological observations of lower mantle isotropy, Geophys. Res. Lett. 22 (1995) 1293–1296.
[42] C.B. Raleigh, Mechanisms of plastic deformation in olivine, J. Geophys. Res. 73 (1968) 5391–5406.
[43] H. Jung, S.I. Karato, Water-induced fabric transitions in olivine, Science 293 (2001) 1460–1463.
[44] C.N. Tomé, G.R. Canova, Self-consistent modeling of heterogeneous plasticity, Chapter 11, in: U.F. Kocks, C.N. Tomé, H.-R. Wenk (Eds.), Texture and Anisotropy. Preferred Orientations in Polycrystals and Their Effect on Materials Properties, 2nd Paperback ed., Cambridge Univ. Press, Cambridge, 2000, pp. 466–510.
[45] P.C. Burnley, W.A. Bassett, T.C. Wu, Diamond-anvil cell study of the transformation mechanism from the olivine to spinel phase in Co_2SiO_4, Ni_2SiO_4, and Mg_2GeO_4, J. Geophys. Res.-Solid Earth 100 (1995) 17715–17723.
[46] J. Chen, D.J. Weidner, J.B. Parise, M.T. Vaughan, P. Raterron, Observation of cation ordering during the olivine–spinel transition in fayalite by in situ synchrotron X-ray diffraction at high pressure and temperature, Phys. Rev. Lett. 86 (2001) 4072–4075.
[47] M. Madon, F. Guyot, J. Peyronneau, J.P. Poirier, Electron-microscopy of high-pressure phases synthesized from natural olivine in diamond anvil cell, Phys. Chem. Miner. 16 (1989) 320–330.
[48] L. Kerschhofer, T.G. Sharp, D.C. Rubie, Intracrystalline transformation of olivine to wadsleyite and ringwoodite under subduction zone conditions, Science 274 (1996) 79–81.
[49] L. Kerschhofer, C. Dupas, M. Liu, T.G. Sharp, W.B. Durham, D.C. Rubie, Polymorphic transformations between olivine, wadsleyite and ringwoodite: mechanisms of intracrystalline nucleation and the role of elastic strain, Miner. Mag. 62 (1998) 617–638.
[50] T.E. Mitchell, Dislocations and mechanical properties of MgO–Al_2O_3 spinel single crystals, J. Am. Ceram. Soc. 82 (1999) 3305–3316.
[51] H.-R. Wenk, G. Canova, A. Molinari, H. Mecking, Texture development in halite: comparison of Taylor model and self-consistent theory, Acta Metall. 37 (1989) 2017–2029.
[52] C. Meade, R. Jeanloz, Yield strength of MgO to 40 GPa, J. Geophys. Res 93 (1988) 3261–3269.
[53] N.L. Carter, H.C. Heard, Temperature and rate-dependent deformation of halite, Am. J. Sci. 269 (1970) 193–249.
[54] J. Chen, D.J. Weidner, M.T. Vaughan, The strength of $Mg_{0.9}Fe_{0.1}SiO_3$ perovskite at high pressure and temperature, Nature 419 (2002) 824–826.
[55] S. Merkel, H.R. Wenk, J. Badro, J. Montagnac, P. Gillet, H.K. Mao, R.J. Hemley, Deformation of $(Mg_{0.9},Fe_{0.1})SiO_3$ perovskite aggregates up to 60 GPa, Earth Planet. Sci. Lett. 209 (2003) 351–360.
[56] J. Sapriel, Domain-wall orientations in ferroelastics, Phys. Rev., B 12 (1985) 5128–5140.

[57] Y. Wang, F. Guyot, A. Yeganeh-Haeri, R.C. Liebermann, Twinning in $MgSiO_3$ perovskite, Science 248 (1990) 468–471.
[58] J. Tullis, T.E. Tullis, Preferred orientation of quartz produced by mechanical Dauphiné twinning: thermodynamics and axial experiments, Am. Geophys. Union Geophys. Monogr. 16 (1972) 67–82.
[59] P. Besson, J.P. Poirier, G.D. Price, Dislocations in $CaTiO_3$ perovskite deformed at high-temperature: a transmission electron microscopy study, Phys. Chem. Miner. 23 (1996) 337–344.
[60] S. Karato, F. Fujino, E. Ito, Plasticity of $MgSiO_3$ perovskite: the results of microhardness tests on single crystals, Geophys. Res. Lett. 17 (1990) 13–16.
[61] J.P. Poirier, S. Beauchesne, F. Guyot, Deformation mechanisms of crystals with perovskite structure, in: A. Navrotsky, D. Weidner (Eds.), Perovskites, Am. Geophys. Union Monogr., 45 (1991) 119–123.
[62] K. Wright, G.D. Price, J.P. Poirier, High-temperature creep of the perovskite $CaTiO_3$ and $NaNbO_3$, Phys. Earth Planet. Inter. 74 (1992) 9–22.
[63] S.-I. Karato, S. Zhang, H.-R. Wenk, Superplasticity in the Earth's lower mantle. Evidence from seismic anisotropy and rock physics, Science 270 (1995) 458–461.
[64] S. Merkel, R.J. Hemley, H.K. Mao, Finite-element modeling of diamond deformation at multimegabar pressures, Appl. Phys. Lett. 74 (1999) 656–665.
[65] Y. Wang, W.B. Durham, I.C. Getting, D.J. Weidner, The deformation-DIA: A new apparatus for high temperature triaxial deformation to pressures up to 15 GPa, Rev. Sci. Instrum. 74 (2003) 3002–3011.
[66] H.-R. Wenk, S. Matthies, R.J. Hemley, H.-K. Mao, J. Shu, The plastic deformation of iron at pressures of the Earth's inner core, Nature 405 (2000) 1044–1047.